The Astrophysical Journal, 885:101 (13pp), 2019 November 10 https://doi.org/10.3847/1538-4357/ab4795

Coronal Cooling as a Result of Mixing by the Nonlinear Kelvin–Helmholtz Instability

Andrew Hillier[1] and Iñigo Arregui[2,3]
[1] CEMPS University of Exeter Exeter EX4 4QF, UK; a.s.hillier@exeter.ac.uk
[2] Instituto de Astrofísica de Canarias Vía Láctea s/n E-38205 La Laguna, Tenerife, Spain
[3] Departamento de Astrofísica Universidad de La Laguna E-38206 La Laguna, Tenerife, Spain
Received 2019 April 25; revised 2019 September 11; accepted 2019 September 23; published 2019 November 5

Abstract

Recent observations show cool, oscillating prominence threads fading when observed in cool spectral lines and appearing in warm spectral lines. A proposed mechanism to explain the observed temperature evolution is that the threads were heated by turbulence driven by the Kelvin–Helmholtz instability that developed as a result of wave-driven shear flows on the surface of the thread. As the Kelvin–Helmholtz instability is an instability that works to mix the two fluids on either side of the velocity shear layer, in the solar corona it can be expected to work by mixing the cool prominence material with that of the hot corona to form a warm boundary layer. In this paper, we develop a simple phenomenological model of nonlinear Kelvin–Helmholtz mixing, using it to determine the characteristic density and temperature of the mixing layer. For the case under study, with constant pressure across the two fluids, these quantities are $\rho_{\rm mixed} = \sqrt{\rho_1 \rho_2}$ and $T_{\rm mixed} = \sqrt{T_1 T_2}$. One result from the model is that it provides an accurate—as determined by comparison with simulation results—determination of the kinetic energy in the mean velocity field. A consequence of this is that the magnitude of turbulence—and with it, the energy that can be dissipated on fast timescales—as driven by this instability can be determined. For the prominence–corona system, the mean temperature rise possible from turbulent heating is estimated to be less than 1% of the characteristic temperature (which is found to be $T_{\rm mixed} = 10^5$ K). These results highlight that mixing, and not heating, is likely to be the cause of the observed transition between cool to warm material. One consequence of this result is that the mixing creates a region with higher radiative loss rates on average than either of the original fluids, meaning that this instability could contribute a net loss of thermal energy from the corona, i.e., coronal cooling.

Key words: instabilities – magnetohydrodynamics (MHD) – Sun: corona – Sun: filaments, prominences – turbulence – waves

1. Introduction

The dissipation of magnetohydrodynamic (MHD) wave energy has been regarded for decades as a relevant agent in explaining the heating of the solar corona; see Arregui (2015), for a recent review. Since first proposed by Ionson (1978), the resonant absorption of surface Alfvén waves has offered a means to transfer wave energy from large to small spatial scales, thus enhancing dissipative processes (Wentzel 1974, 1978, 1979; Hollweg 1978). Theoretical and numerical advances have recently shown that the nature of the resonantly damped transverse kink wave (Goossens et al. 2009) and its associated nonlinear dynamics leads to the development of Kelvin–Helmholtz (KH) unstable flows (Terradas et al. 2008, 2018; Antolin et al. 2014, 2015, 2016, 2017). The instability arises in connection with resonant absorption processes because of the creation of a shear velocity pattern around the resonance, but owes its existence to the presence of a discontinuous shear flow even in models with a density jump at the boundary of the waveguide. It operates by extracting energy from the large-scale dynamics to spread it among different spatial scales and locations. The cause of the heating, though, is still under investigation (Magyar & Van Doorsselaere 2016; Howson et al. 2017; Karampelas et al. 2017; Antolin et al. 2018). It has been shown in some cases that mixing, as well as heating, plays a dominant role in the thermal evolution (e.g., Magyar & Van Doorsselaere 2016; Karampelas et al. 2017).

Only recently has observational evidence about these small-scale physical processes begun to be pursued. Prominence plasmas offer a natural laboratory in this context, because of the occurrence of complex oscillatory and flow patterns at both large scales (Berger et al. 2008; Hillier et al. 2013) and in their fine structure (Okamoto et al. 2007, 2015). In particular, recent observations by Okamoto et al. (2015), using the Interface Region Imaging Spectrograph (IRIS; De Pontieu et al. 2014) and *Hinode* Solar Optical Telescope (SOT; Tsuneta et al. 2008), found oscillations of prominences threads that display velocity features consistent with resonant absorption. These threads were often found to fade from the cool passbands on Mg II K (observed by IRIS) and Ca II H (observed by *Hinode* SOT), while becoming brighter in warmer (Si IV) IRIS passbands. Antolin et al. (2015) simulated these processes, showing that the concentration of the wave energy onto the surface of the flux tube produced shear flows large enough to develop an instability. The key process they proposed to be behind the observed temperature evolution was heating as a result of turbulence driven by the magnetic Kelvin–Helmholtz instability. This mechanism has also been found in simulations of oscillating coronal loops (Terradas et al. 2008).

The KH instability breaks up shear flows by creating vortices at the shear layer (Chandrasekhar 1961), mixing the two regions together. These vortices may themselves break up into turbulence via secondary 3D instabilities. With the inclusion of magnetic fields, magnetic tension works to suppress the KH instability. Therefore, the most unstable modes become those that vary little along the field. This instability has been found to occur in a number of different situations in the solar atmosphere, including in the interaction between prominences and bubbles that form below them (Berger et al. 2010, 2017; Ryutova et al. 2010), in internal prominence motions (Hillier & Polito 2018; Yang et al. 2018), and as a result of eruptions in

the solar atmosphere (Foullon et al. 2011; Ofman & Thompson 2011; Möstl et al. 2013). Soler et al. (2010) investigated how this instability develops on the surface of a rotating flux tube, a model used because of its geometrical connection to coronal loops; they found that the fundamental physics of the linear instability are not greatly altered by the change in geometry. The studies of Hillier et al. (2019) and Barbulescu et al. (2019) highlighted the important role the oscillatory nature of the flow in wave-driven KHi could have in determining stability, with both the KHi and resonance-induced parametric instabilities existing. Once the linear instability has developed, nonlinearities form; it is in this nonlinear stage that the important processes of heating and mixing are driven.

The nonlinear stage of the instability is where the dynamics that are key to explaining the observations should be occurring. Ryu et al. (2000) investigated the 3D evolution of the MHD KHi, finding the KHi vortices could become disrupted, resulting in highly turbulent and efficient mixing of the two layers. A detailed 2D analysis of the disruption process of a KHi vortex via magnetic reconnection was presented in Mak et al. (2017), finding that significant disruption would occur when $M^2\mathrm{Rm} = O(1)$ (M is the Alfvén Mach number and R_m is the magnetic Reynolds number). Matsumoto & Seki (2010) studied the nonlinear evolution of high density-contrast MHD KHi in 2D simulations, finding that large asymmetric mixing layers were formed. This implies that, for situations in the solar atmosphere, both the magnetic field and density contrast can be important for determining the mixing dynamics.

There are three questions to which the answer would provide information crucial to understanding the role of the KH instability in heating the solar corona: (1) What is the temperature in the KH layer achieved purely from mixing? (2) How much heating can be driven by the instability? (3) On what timescales does this heating occur? In this paper, we present a phenomenological model of a turbulent MHD Kelvin–Helmholtz mixing layer that we use to provide answers to these three questions. We also use 3D MHD simulations to confirm the predictions of the model and to highlight areas in which the model can be improved.

2. Modeling the Nonlinear Kelvin–Helmholtz Instability Mixing Layer

Our model aims at investigating the nonlinear solution of the magnetic KH instability as pertinent to a surface flow on an oscillating flux tube. For simplicity, we consider a phenomenological model consisting of a plane-parallel shear flow defined by:

$$V_x(y) = \begin{cases} V_1 & \text{if } y < 0; \\ V_2 & \text{if } y > 0 \end{cases}, \tag{1}$$

$$\rho(y) = \begin{cases} \rho_1 & \text{if } y < 0; \\ \rho_2 & \text{if } y > 0 \end{cases}, \tag{2}$$

$$p(y) = p, \tag{3}$$

$$B_z(y) = B, \tag{4}$$

which is a discontinuous velocity field creating a shear layer at $y = 0$ (e.g., Figure 1) composed of two uniform layers that have their own uniform density, but the gas pressure and magnetic field strengths are constant throughout the domain, which ensures equilibrium. The initial velocity profile is shown in Figure 1.

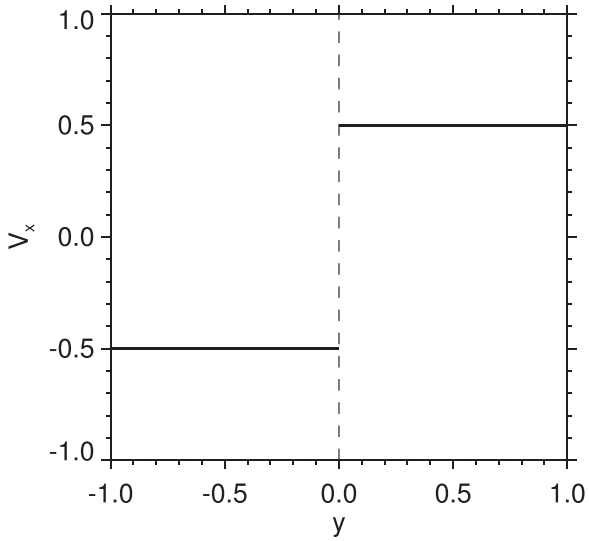

Figure 1. Plot of the initial velocity distribution (normalized so that $\Delta V = 1$).

2.1. The Position of the Mixing Layer

For the linear instability with a discontinuity in the velocity and density at $y = 0$, the instability is centered at $y = 0$, with the eigenfunction decaying from there as $\exp(-k|y|)$ (e.g., Chandrasekhar 1961). However, the nonlinear evolution of the instability is not required to obey the same rules. Therefore, the initial step to understanding the nonlinear mixing is to determine where a mixing layer would be centered. Here, our first assumption is introduced: we assume that the mixing works in the way that most efficiently uses the free energy associated with the initial flow. Therefore, for a mixing layer of width across the shear layer of $2l$, it will be centered at the position Y that maximizes the kinetic energy associated with the shear flow.

As an aside, it is worth noting that the length scales of the vortical/turbulent structures in the direction of the shear flow generally control the width $2l$. Using as a guide the Kelvin–Stuart cat's eye vortex flow (Kelvin 1880; Stuart 1967), which is a steady-state flow solution producing a string of vortices given by

$$[V_x,\, V_y] = V_\infty \frac{[\sinh(ky),\, \varepsilon \sin(ky)]}{\cosh(ky) + \varepsilon \cos(kx)}, \tag{5}$$

where V_∞ is the velocity of the flow as $y \to \infty$, $k = 2\pi/l_\mathrm{flow}$, with l_flow being the length of the vortex in the direction of the shear flow, and ε being the parameter that controls the localization of the vorticity. Based on this solution, we expect that $2l < l_\mathrm{flow}$, with $2l \approx l_\mathrm{flow}/2$ being a common ratio. As the length scales associated with the vortices/turbulence grow linearly with time (e.g., Winant & Browand 1974), the width should keep on increasing until geometric effects cause it to saturate.

Determining the position Y has one major difficulty: the kinetic energy measured for each component of a shear flow will depend on the reference frame in which the flow is being observed. Therefore, different initial conditions would result in different layer positions. However, it should be expected that, in situations with the same magnitude of density and velocity jump at $y = 0$ but with different velocity values, the properties of the solution should not change, i.e., the problem is Galilean

invariant. Therefore, the question is: what is the correct reference frame to view the problem so that the kinetic energy available is the kinetic energy that can be used by the nonlinear instability? For this, the natural choice is to put the velocities into the zero-momentum reference frame, because it results in the removal of any mean advection in the layer.

If we take a mixing layer of width $2l$ that is centered on Y, where Y is in the range $[-l, l]$, then a zero-momentum reference frame can be calculated for that layer. This is given by integrating the momentum across the layer and setting the result to zero, i.e.:

$$\frac{1}{\rho_1+\rho_2}\left(\int_{Y'-1}^{0}\rho_1 V_1 dy' + \int_{0}^{Y'+1}\rho_2 V_2 dy'\right) = 0, \quad (6)$$

where $Y' = Y/l$. On solving this integral, we have:

$$\alpha_1 V_1(1-Y') + \alpha_2 V_2(1+Y') = 0, \quad (7)$$

where $\alpha_{1,2} = \rho_{1,2}/(\rho_1+\rho_2)$ Using the identity $\Delta V \equiv V_1 - V_2$ we can define V_1 and V_2 as:

$$V_1 = -\frac{\alpha_2 \Delta V(1+Y')}{Y'(\alpha_1-\alpha_2)-1}, \quad (8)$$

$$V_2 = \frac{\alpha_1 \Delta V(1-Y')}{Y'(\alpha_1-\alpha_2)-1}. \quad (9)$$

From this, we can show that the mean kinetic energy (KE) for the layer in the zero-momentum frame is given by:

$$\mathrm{KE} = \rho_{\mathrm{av}}\left[\alpha_1 V_1^2\frac{1-Y'}{2} + \alpha_2 V_2^2\frac{1+Y'}{2}\right] = \frac{\rho_{\mathrm{av}}\alpha_1\alpha_2\Delta V^2(Y'-1)(Y'+1)}{2[Y'(\alpha_1-\alpha_2)-1]}, \quad (10)$$

where ρ_{av} is the average of the densities of the two layers. For example, the mean kinetic energy for the band from $y = -2l$ to 0 (centered on $Y = -l$), when put in the zero-momentum frame of reference, has no kinetic energy because there is no velocity shear in this region. The same can be said for the region $y = 0$ to $2l$ (centered on $Y = l$). The mean kinetic energy peaks at somewhere between these two values, at the point:

$$Y'_{\mathrm{max}} = \frac{1-\sqrt{4\alpha_2\alpha_1}}{\alpha_1-\alpha_2} = \frac{\sqrt{\alpha_1}-\sqrt{\alpha_2}}{\sqrt{\alpha_1}+\sqrt{\alpha_2}}. \quad (11)$$

A key point here is that this shift is completely independent of the magnitude of the velocity shear; it is a function only of the normalized densities. This gives the two velocities in this reference frame as:

$$V_1 = \frac{\alpha_2\Delta V(2\alpha_1-\sqrt{4\alpha_1\alpha_2})}{\sqrt{4\alpha_1\alpha_2}(\alpha_1-\alpha_2)} = \frac{\Delta V\sqrt{\alpha_2}}{\sqrt{\alpha_1}+\sqrt{\alpha_2}}, \quad (12)$$

$$V_2 = -\frac{\alpha_1\Delta V(\sqrt{4\alpha_1\alpha_2}-2\alpha_2)}{\sqrt{4\alpha_1\alpha_2}(\alpha_1-\alpha_2)} = -\frac{\Delta V\sqrt{\alpha_1}}{\sqrt{\alpha_1}+\sqrt{\alpha_2}}. \quad (13)$$

This leads the maximum value for the mean KE in this layer to be:

$$\mathrm{KE}_{\mathrm{max}} = \frac{\rho_{\mathrm{av}}\Delta V^2\alpha_1\alpha_2}{(\sqrt{\alpha_1}+\sqrt{\alpha_2})^2}. \quad (14)$$

Figure 2 shows the distribution of KE for given layer positions for $\alpha_1 = 1/11$. The position of the peak value, as determined in Equation (11), is shown by the vertical line. One interesting property of this peak is that it is achieved when the layer is placed such that the initial kinetic energy distribution becomes continuous (i.e., the kinetic energy is the same on either side of the discontinuity).

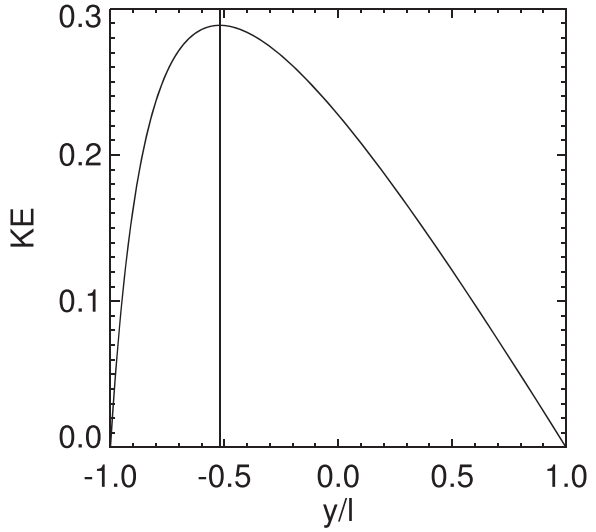

Figure 2. Plot of the kinetic energy (using the normalized density and velocity profiles) against Y'. Vertical solid line gives the position of the peak value as given in Equation (11).

2.2. Density, Pressure, Magnetic Field, and Temperature

Once the position of the layer has been determined, the next step is to estimate the values of the average density, pressure, and magnetic field in the mixed layer. To do this, we will consider conserved quantities in MHD flows, i.e., conservation of mass, momentum, energy, and magnetic flux, to determine the characteristic values of the density, pressure, and magnetic field as achieved by mixing.

For a mixing layer consisting of a layer of width $2l$, the characteristic density that results from mixing (ρ_{mixed}) can be calculated using conservation of mass from the two densities (ρ_1 and ρ_2 respectively). That is to say, for a layer of width $2l$ centered at Y, the following equality must hold:

$$\rho_1\int_{-l+Y}^{0} dy + \rho_2\int_{0}^{l+Y} dy = \rho_{\mathrm{mixed}}\int_{-l+Y}^{l+Y} dy = 2l\rho_{\mathrm{mixed}}. \quad (15)$$

This gives:

$$\rho_{\mathrm{mixed}} = \frac{\rho_1(1-Y')+\rho_2(1+Y')}{2}, \quad (16)$$

where, as before, $Y' = Y/l$. At Y'_{max}, this equals:

$$\rho_{\mathrm{mixed}} = \rho_{\mathrm{av}}\sqrt{4\alpha_1\alpha_2} = \sqrt{\rho_1\rho_2}. \quad (17)$$

The mixed pressure p_{mixed} follows from an averaging process similar to that used for the density. First, we note that, based on the first law of thermodynamics, we expect:

$$\delta U + \delta W = \delta Q, \quad (18)$$

where δU is the change in internal energy, δW is the work done, and δQ is the heating. In the case of no dissipation, then enthalpy is conserved, i.e., $\delta U + \delta W = 0$ (e.g., Vallis 2017). In

the regime where compressive effects are small, this then becomes $\delta U \approx 0$; for an adiabatic process, it reduces to a conservation of total pressure equation. As we have assumed an initial constant pressure, this implies that the mixing gives

$$p_{\rm mixed} = p. \tag{19}$$

As we shall see later, the latter assumption of small compressibility can be violated, but this provides a good starting point to estimate the characteristic pressure in the mixing layer—even though further work is necessary to make it completely accurate in all cases. This implies that a measure of the temperature in this mixed region can be given as

$$T_{\rm mixed} = \frac{p_{\rm mixed}\,\mu}{\rho_{\rm mixed} R_{\rm g}}, \tag{20}$$

where μ is the mean molecular mass and $R_{\rm g}$ is the gas constant. Therefore:

$$T_{\rm mixed} = \sqrt{T_1 T_2}. \tag{21}$$

The characteristic field strength in the mixing layer is necessarily determined by conservation of flux. This again leads to a simple averaging to determine the field strength—being constant in the domain, it just gives:

$$B_{\rm mixed} = B. \tag{22}$$

2.3. Developing a Simple Model to Estimate the Kinetic Energy of the Mean Flow

One aim of this paper is to estimate the proportion of the energy that is extracted from the mean flow, to create an upper bound on the amount of energy that can exist in turbulent flows. To do this, we must first make a model of the mean velocity field that can be used to estimate the kinetic energy that remains in the mean flow (i.e., is not available for turbulent motions), and then whatever is left over can be used as the upper limit for the turbulent kinetic energy.

2.3.1. Mean Density and Velocity Profiles

The profile across the mixing layer of the averaged density and velocity would provide important information on the kinetic energy distribution in the mixing layer. However, to develop an approximation of these profiles, further constraints and assumptions are necessary. The mixing layer has been placed into its zero-momentum frame, so any velocity profile needs to be such that this condition is maintained. On top of this, conservation of mass of the layer must be observed.

To model $\langle\rho\rangle$ and $\langle v_x\rangle$, we develop an approximate polynomial solution, based on basic rules developed for the mixing layer. We first apply the condition that both the $\langle\rho\rangle$ and $\langle\rho\rangle\langle v_x\rangle$ are continuous; i.e., at either edge of the mixing layer, they take the values of the background density and flow. This is ρ_1 and ρ_2 for the density, and the results given in Equations (12) and (13) for the velocity. Conservation of mass demands that:

$$\int_{-1+Y'}^{1+Y'} \langle\rho\rangle\, dy' = 2\sqrt{\rho_1\rho_2}, \tag{23}$$

where $dy' = dy/l$. The conservation of momentum is more complex, with the true statement of the conservation of momentum in the layer giving:

$$\int_{-1+Y'}^{1+Y'} \langle\rho\rangle\langle v_x\rangle + \langle\rho' v_x'\rangle\, dy' = 0, \tag{24}$$

where the primes denote the fluctuating component. We assume that the fluctuations in the density and velocity fields are essentially uncorrelated, meaning that the magnitude of the fluctuating term goes to zero when integrated across the layer. Thus, our condition becomes:

$$\int_{-1+Y'}^{1+Y'} \langle\rho\rangle\langle v_x\rangle\, dy' = 0. \tag{25}$$

We then require that the distributions of $\langle\rho\rangle$ and $\langle\rho\rangle\langle v_x\rangle$ vary monotonically. We also prescribe that, as the mixing of the momentum happens in conjunction with the mixing of the density, the y position where $\langle\rho\rangle = \rho_{\rm mixed}$ is the same as the position where $\langle\rho\rangle\langle v_x\rangle = 0$. Finally, as has been key to the derivations performed so far, we have assumed that the nonlinear dynamics works to release as much of the kinetic energy from the mean flow as possible, i.e., that

$$\int_{-1+Y'}^{1+Y'} \tfrac{1}{2}\langle\rho\rangle\langle v_x\rangle^2\, dy' \tag{26}$$

is minimized.

After applying these rules, third-order polynomials for $\langle\rho\rangle$ and $\langle v_x\rangle$ are determined under the constraint of energy minimization. The steps applied to this minimization are as follows:

1. Using a uniform grid, the mixing layer is discretized into 1001 grid points.
2. Taking each point in the grid in turn as the point where $\langle\rho\rangle = \sqrt{\rho_1\rho_2}$, the polynomial for the density distribution is determined using the rules on the total density and the density at each end of the layer.
3. For a density distribution where the gradient is positive throughout the layer, the velocity distribution is then calculated.
4. Using the grid point where $\langle\rho\rangle = \sqrt{\rho_1\rho_2}$, we set $\langle v_x\rangle = 0$ and determine the $\langle v_x\rangle$ solution based on the other constraints on the momentum listed above.
5. All grid points on the grid are cycled through, and the grid point selected will be the one that satisfies the constraints on the distribution and is associated with the least energy in the mean flow.

The approximate solutions are shown in Figure 3, with the density distribution for our model using three different values of α_1 in panel (a) and the same for the velocity in panel (b). Aside from the shift in the position of the layer, there are some interesting effects from the changing of the density contrast—the most important being that the density distribution becomes heavily skewed. This results in the point where $\langle\rho\rangle = \rho_{\rm mixed}$ becoming closer and closer to the high-density edge of the mixing layer. It is worth noting that the distribution of the $\alpha_1 = 1/2$ solution for $\langle v_x\rangle$ is similar to that of the error function, which is important because this is the classic solution (confirmed via comparison with experimental data) used to explain turbulence developing between two flows (e.g., Winant & Browand 1974). However, there is one important difference:

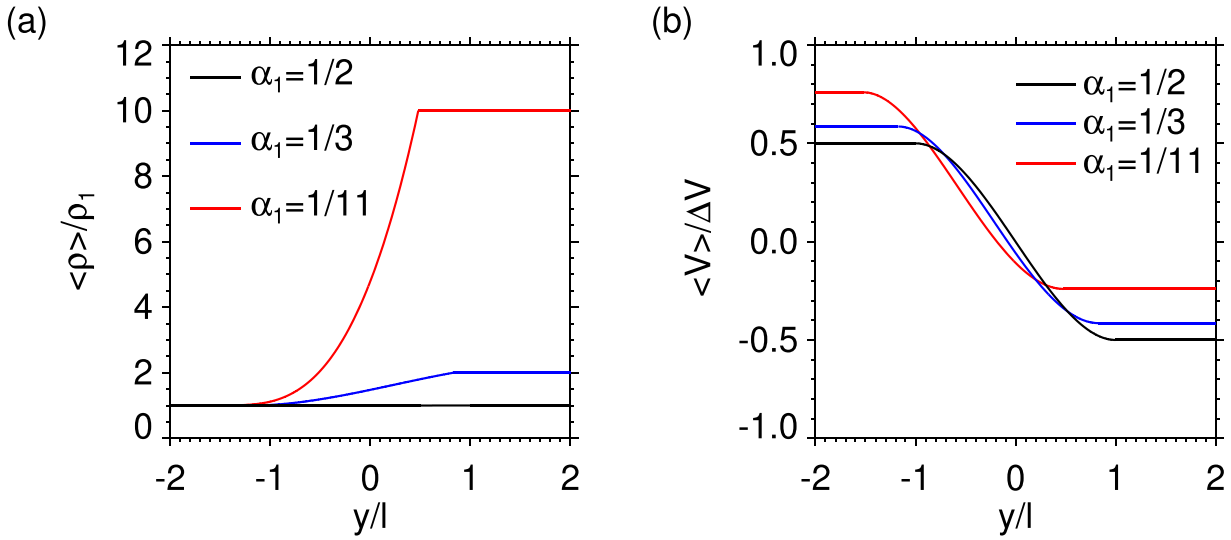

Figure 3. Density and velocity field of the mixed region for a calculation of $\Delta V = 1$. The red line has $\alpha_1 = 1/11$, the blue line has $\alpha_1 = 1/3$, and the black line has $\alpha = 1/2$.

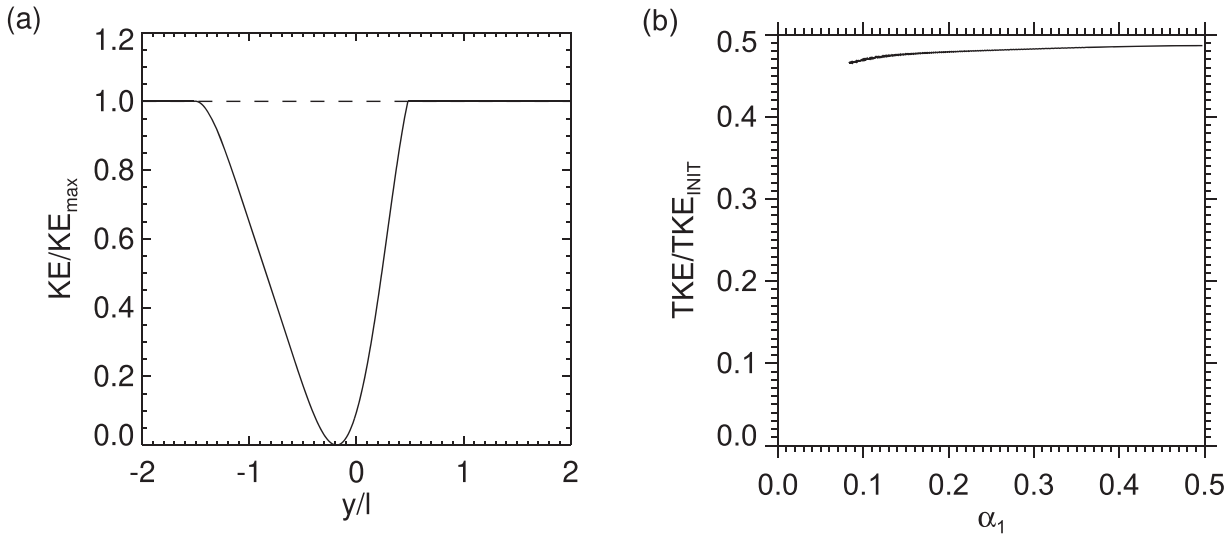

Figure 4. Plot of the kinetic energy of the mean flow normalized by the value of the kinetic energy outside of the mixing layer for the case where $\alpha_1 = 1/11$. The dashed line gives the initial kinetic energy distribution (left). Also plotted is the ratio of the mean-flow total kinetic energy (TKE) to the initial total kinetic energy ($\mathrm{TKE_{INIT}}$) against α_1.

as our model is separated into three layers, if a continuous, smooth function were to be used to explain the distribution, it would be nonanalytic.

The kinetic energy distribution in the mixing layer is given by:

$$\mathrm{KE_{mixed}}(y) = \tfrac{1}{2}\langle\rho\rangle\langle v_x\rangle^2. \tag{27}$$

Because of the continuity of the density and velocity, this is also a continuous distribution. An example of the kinetic energy distribution, in this case for $\alpha_1 = 1/11$, is presented in panel (a) of Figure 4. The total kinetic energy of this mean component is also relatively simple to calculate. Using $\langle\rho\rangle$ and $\langle x\rangle$ and integrating over y gives:

$$\mathrm{TKE} = \frac{1}{2}\int_{-1+Y'}^{1+Y'}\langle\rho\rangle\langle v_x\rangle^2 dy'. \tag{28}$$

This can be compared to the initial kinetic energy of the band, i.e., the energy before mixing:

$$\mathrm{TKE_{INIT}} = \rho_{\mathrm{mixed}}\frac{\Delta V^2(\alpha_1\alpha_2)^{1/2}}{(\sqrt{\alpha_1}+\sqrt{\alpha_2})^2}. \tag{29}$$

The comparison between these two is presented for a range of α_1 values in panel (b) of Figure 4, where it is clear that this ratio is always less than 0.5 and becoming smaller as α_1 tends to zero. Therefore, we can approximate TKE by

$$\mathrm{TKE} \approx \frac{1}{2}\rho_{\mathrm{mixed}}\frac{\Delta V^2(\alpha_1\alpha_2)^{1/2}}{(\sqrt{\alpha_1}+\sqrt{\alpha_2})^2}. \tag{30}$$

We note that the range of α_1 used in panel (b) of Figure 4 is reduced because the accuracy of the third-order polynomial approximation deteriorates at small α_1 values, due to the low order of the polynomial used. This implies that further constraints exist on the distributions, likely to be related to the various orders

of the derivatives of the density, momentum, and kinetic energy at the edges of the layer, which could be used to extend this approximation to higher order—and with that, lower α_1.

2.4. Estimate of the Fluctuating Energy Component

The next question we would like to approach is: how much energy is there available to dissipate via the turbulent creation of small scales? In other words, what energy is there available for heating from the fluctuations of the velocity field (and in an MHD system, the magnetic field) around their average values? The density—and with it, the temperature—of the mixed layer does not depend of the amount of free kinetic or magnetic energy there is to dissipate; it is purely based on the density and temperatures of the regions before they are mixed. However, the total dissipation that can occur is highly dependent on these.

In Section 2.3.1, we formulated the mean velocity field of the mixed region. This velocity field is related to the average velocity profile and does not include the fluctuating component of the velocity field, often referred to as the turbulent component. The profile shows the lowest energy state the velocity field can reach without further thickening of the mixing layer through development of larger vortices or through viscous dissipation, i.e., it is related to how much energy the instability can release through turbulent motions. Therefore, the energy held in the fluctuations can be estimated by the initial energy available for the instability minus the newly developed mean kinetic energy profile. The total kinetic energy of the fluctuating component of the velocity field is given as:

$$\mathrm{TKE}_{\mathrm{turb}} \sim \frac{1}{2}\rho_{\mathrm{mixed}}\frac{\Delta V^2(\alpha_1\alpha_2)^{1/2}}{(\sqrt{\alpha_1}+\sqrt{\alpha_2})^2}, \tag{31}$$

which is minimized for large density differences. The average turbulent kinetic energy across the layer is given as:

$$\overline{\mathrm{KE}}_{\mathrm{turb}} \sim \frac{1}{4}\rho_{\mathrm{mixed}}\frac{\Delta V^2(\alpha_1\alpha_2)^{1/2}}{(\sqrt{\alpha_1}+\sqrt{\alpha_2})^2}. \tag{32}$$

The characteristic magnitude of the velocity fluctuations is given by:

$$V_{\mathrm{turb,rms}} \sim \sqrt{\frac{2}{\rho_{\mathrm{mixed}}}\overline{\mathrm{KE}}_{\mathrm{turb}}} \sim \sqrt{\frac{1}{2}}\frac{\Delta V(\alpha_1\alpha_2)^{1/4}}{(\sqrt{\alpha_1}+\sqrt{\alpha_2})}. \tag{33}$$

The average increase in internal energy of an ideal gas as a result of processes other than mixing is given by $\overline{\Delta p}/(\gamma-1)$, i.e., the heating must come from the dissipation of the turbulent kinetic energy. Therefore, based on energy conservation, we know:

$$\begin{aligned}\frac{\overline{\Delta T}}{T_{\mathrm{mixed}}} \sim \frac{\overline{\Delta p}}{p_{\mathrm{mixed}}} &\approx \frac{1}{4}(\gamma-1)\frac{(\alpha_1\alpha_2)^{1/2}\Delta V^2}{(\sqrt{\alpha_1}+\sqrt{\alpha_2})^2}\frac{\rho_{\mathrm{mixed}}}{p_{\mathrm{mixed}}}\\ &= \frac{\gamma}{4}(\gamma-1)\frac{(\alpha_1\alpha_2)^{1/2}}{(\sqrt{\alpha_1}+\sqrt{\alpha_2})^2}\frac{\Delta V^2}{C_{\mathrm{S,mix}}^2}\\ &\sim \frac{1}{4}\frac{(\alpha_1\alpha_2)^{1/2}}{(\sqrt{\alpha_1}+\sqrt{\alpha_2})^2}\frac{\Delta V^2}{C_{\mathrm{S,mix}}^2}\\ &\leqslant \frac{1}{16}\frac{\Delta V^2}{C_{\mathrm{S,mix}}^2} = \frac{1}{16}M^2,\end{aligned} \tag{34}$$

where γ is the adiabatic index, $C_{\mathrm{S,mix}}$ is the characteristic sound speed of the mixed region where the energy is being dissipated, and M is the Mach number. Therefore, if we know the velocity shear and can estimate the sound speed of the mixed region, then we can give a bound for the average heating. If the density ratio is also relatively well-constrained, then this can be used to accurately estimate the heating.

2.4.1. Estimating the Effect of the Turbulent Pressures

Both the dynamic and magnetic pressures that result from the fluctuating velocity and magnetic field, respectively, in the mixing layer can work to expand the mixing layer by acting to add to the total pressure of that region. The magnitude of these two turbulent pressures is intrinsically related to the amount of kinetic energy that is taken from the large-scale shear flow and put into the turbulent components of the velocity and magnetic field. The importance of these turbulent pressures can be estimated using the characteristic Mach number of the instability or the characteristic Alfvén Mach number of the instability, depending on whether the system has high or low β, where if these characteristic numbers are small then it can be expected that the effect of turbulent pressure is negligible. See the results in Section 2.4 for estimates of the kinetic energy that can be transferred to these fluctuations (and with it, an approximation of the total turbulent pressure they can create). As the turbulent pressures are representative of the energy available for dissipation, similar arguments can be formed for loss of force balance through the pressure increase through dissipative heating.

2.5. Timescales for Mixing

The previous parts of this section focused on the quantities of the mixed layer. These are the quantities that the mixing is driving the system to achieve, and they represent the mean values of the layer during the mixing process. However, there remains a very important question: what is the timescale over which the mixing occurs?

To answer this, it is necessary to have a measure of the magnitude of the velocity fluctuations in the mixing layer, which can be taken from the fluctuating energy component. Using the estimate for the turbulent velocity rms given in Equation (33), the mixing time can be approximated by an eddy turnover time:

$$\tau_{\mathrm{mixing}} \approx \frac{2l}{V_{\mathrm{turb,rms}}} \geqslant \frac{2l}{\Delta V}\sqrt{2}\frac{\sqrt{\alpha_1}+\sqrt{\alpha_2}}{(\alpha_1\alpha_2)^{1/4}}, \tag{35}$$

which gives a measure of how long it takes to mix the region.

This mixing time will strongly correlate to the dissipation timescale in the limit where $\tau_{\mathrm{mixing}} \ll \tau_{\mathrm{viscous}}$. In a turbulent system, which is likely to form under the previously stated conditions, the nature of the cascade implies that the longest timescales are those at the largest scale. Therefore, as with the mixing, the dissipation rate is connected (albeit in a complex fashion) to the timescales at the largest scale. As such, the mixing time can also be used as a very approximate measure of the lower limit of the dissipation timescale in turbulent mixing.

The addition of a magnetic field to the problem adds a number of other considerations. In flows with high Lundquist numbers, the fluid is strongly tied to the magnetic field, which inhibits mixing. Therefore, as discussed in the introduction, to have quick efficient mixing, magnetic reconnection leading to the disruption of vortices becomes necessary. In the 3D simulations of Antolin et al. (2015), many current sheets were found to form (a necessary condition for magnetic reconnection), showing that

mixing is possible in the regime we are interested. Therefore, assuming that the current sheets form on an eddy-turnover timescale, i.e., the timescale we have estimated, this will still hold as an approximate mixing timescale.

3. Numerical Simulations of Kelvin–Helmholtz Mixing

To both confirm the key predictions and evaluate the limits of this model, we present the results from a 3D MHD simulation of Kelvin–Helmholtz mixing.

3.1. Setup

Using the (PI P) code (Hillier et al. 2016), we solve the nondimensionalized ideal MHD equations:

$$\frac{\partial \rho}{\partial t} + \nabla \cdot (\rho \boldsymbol{v}) = 0, \tag{36}$$

$$\frac{\partial}{\partial t}(\rho \boldsymbol{v}) + \nabla \cdot \left(\rho \boldsymbol{v}\boldsymbol{v} + P\boldsymbol{I} - \boldsymbol{B}\boldsymbol{B} + \frac{\boldsymbol{B}^2}{2}\boldsymbol{I} \right) = 0, \tag{37}$$

$$\frac{\partial}{\partial t}\left(e + \frac{B^2}{2} \right) + \nabla \cdot [\boldsymbol{v}(e + P) - (\boldsymbol{v} \times \boldsymbol{B}) \times \boldsymbol{B}] = 0, \tag{38}$$

$$\frac{\partial \boldsymbol{B}}{\partial t} - \nabla \times (\boldsymbol{v} \times \boldsymbol{B}) = 0, \tag{39}$$

$$\nabla \cdot \boldsymbol{B} = 0, \tag{40}$$

$$e \equiv \frac{P}{\gamma - 1} + \frac{1}{2}\rho v^2. \tag{41}$$

This system of equations has been nondimensionalized in the following way: the velocity $\boldsymbol{v}$ has been nondimensionalized using the sound speed C_s, the density ρ by a reference density ρ_0, and the length scale by an arbitrary length L. Therefore, time t is nondimensionalized by $L/C_s = \tau_D$, the pressure P by $C_s^2 \rho_0$, and the magnetic field $\boldsymbol{B}$ by $B_0/\sqrt{4\pi} = C_s\sqrt{\rho_0}$. Here, γ is the adiabatic index and β is plasma β (the ratio of gas to magnetic pressure calculated using the total gas pressure of the fluids). We assume the ideal gas law, which in nondimensional form becomes $T = \frac{P\gamma}{\rho}$.

The scheme used is a fourth-order central difference scheme using a four-step Runge–Kutta scheme for the time integration. For stability of the scheme, we employ the artificial viscosity/diffusion as described in Rempel et al. (2009). Because this is a conservative scheme, the artificial dissipation results in an internal energy increase matching the amount of energy that has been dissipated.

The initial conditions used for the present simulation attempt to, as closely as possible, both match the model developed and include the general characteristics in terms of speed and density of the flows believed to exist in the observed prominence threads. Initial conditions for MHD simulations are given by:

$$V_x(y) = V_1 + \frac{\Delta V}{2}\left(\tanh\left(\frac{y}{0.003} \right) + 1 \right), \tag{42}$$

$$\rho(y) = \rho_1 + \frac{\rho_2 - \rho_1}{2}\left(\tanh\left(\frac{y}{0.003} \right) + 1 \right), \tag{43}$$

$$p(y) = p_1 = \frac{1}{\gamma}, \tag{44}$$

$$B_z(y) = B_1 = \sqrt{\frac{2}{\gamma\beta}}, \tag{45}$$

where $\rho_1 = 1$, $\rho_2 = 10$, $p_1 = 1/\gamma$, $V_1 = 10/11 \times \sqrt{0.1}$, and $\Delta V = \sqrt{0.1}$ (i.e., the sound speed of the cool region), which initiates the instability in approximately its linear reference frame (which is different from the frame we predict the nonlinear dynamics will be at rest). We set the plasma β to be $\beta = 2p_1/B_1^2 = 0.3$ and take $\gamma = 5/3$. The instability is seeded with a random noise perturbation in v_y at the level of $0.01\Delta V$.

The simulation is solved in the spatial domain of $x = [-0.4, 0.4]$, $y = [-1.5, 0.5]$ and $z = [-8, 8]$ using $160 \times 400 \times 800$ grid points. Here, we have taken the length of the z direction to be much greater than that of either the x or y directions. This is chosen because, without a sufficient length along the magnetic field, the vortices will not be able to sufficiently wrap up the magnetic field and will not disrupt, as there are insufficient currents for magnetic reconnection to take place. The length scale required for disruption to be possible can be estimated by requiring that the rotation rate of the vortex is greater than the frequency of an Alfvén wave, i.e.,:

$$\frac{V_{\mathrm{turb,rms}}}{2l} > \frac{V_A}{L}, \tag{46}$$

where $2l$ is the width of the vortex, L is the length along the magnetic field and $V_A = B_1/\sqrt{\rho_{\mathrm{mixed}}}$. Therefore,

$$L > \frac{V_A 2l}{V_{\mathrm{turb,rms}}} = \frac{B_1}{\sqrt{2\rho_{\mathrm{av}}}}\frac{2l}{\Delta V} 2l \frac{\sqrt{2}\,(\sqrt{\alpha_1} + \sqrt{\alpha_2})}{\sqrt{\alpha_1\alpha_2}} \approx 11.8, \tag{47}$$

where we have assumed a mixing layer width of $2l = 1$. As the length of our z direction is greater than 11.8, we expect the vortices to become disrupted.

In this calculation, we use the following boundary conditions: the x and z boundaries are set as a periodic boundary, with a symmetric boundary that cannot be penetrated by the magnetic field for the y boundary.

3.2. Simulation Results

Figure 5 shows the contour plots of the temperature distribution in the x–y plane at $z = 0$. These plots show the temperature structure at four different times ($t = 0$, 20, 40, and 60) covering the initial conditions through the early nonlinear stages toward a layer that is becoming well-mixed (note that the lack of coherent vortex structures here is a sign that they have become disrupted). Here, we can see that there is an increase in temperature in the region $y > 0$, and we will determine whether this is created by mixing or heating.

Figure 6 shows the x–z averaged (a) density ($\langle\rho\rangle$), (b) x velocity ($\langle v_x\rangle$), and (c) mean flow kinetic energy ($\langle\rho\rangle\langle v_x\rangle^2/2$) profiles across the mixing region at $t = 60$ (solid black line). Before looking at the distributions and the characteristic values of these quantities in the mixing layer, we need to state how we determined the position of the mixing layer. For this, we look at the distribution of $\langle\rho\rangle$ and determine the point where the density departs from the minimum level by 1%. This gives the position of the $y < 0$ end of the mixing layer. As the shift in the layer is purely a function of α_1 and α_2, this is determined by the initial conditions to be (in normalized units) approximately -0.52.

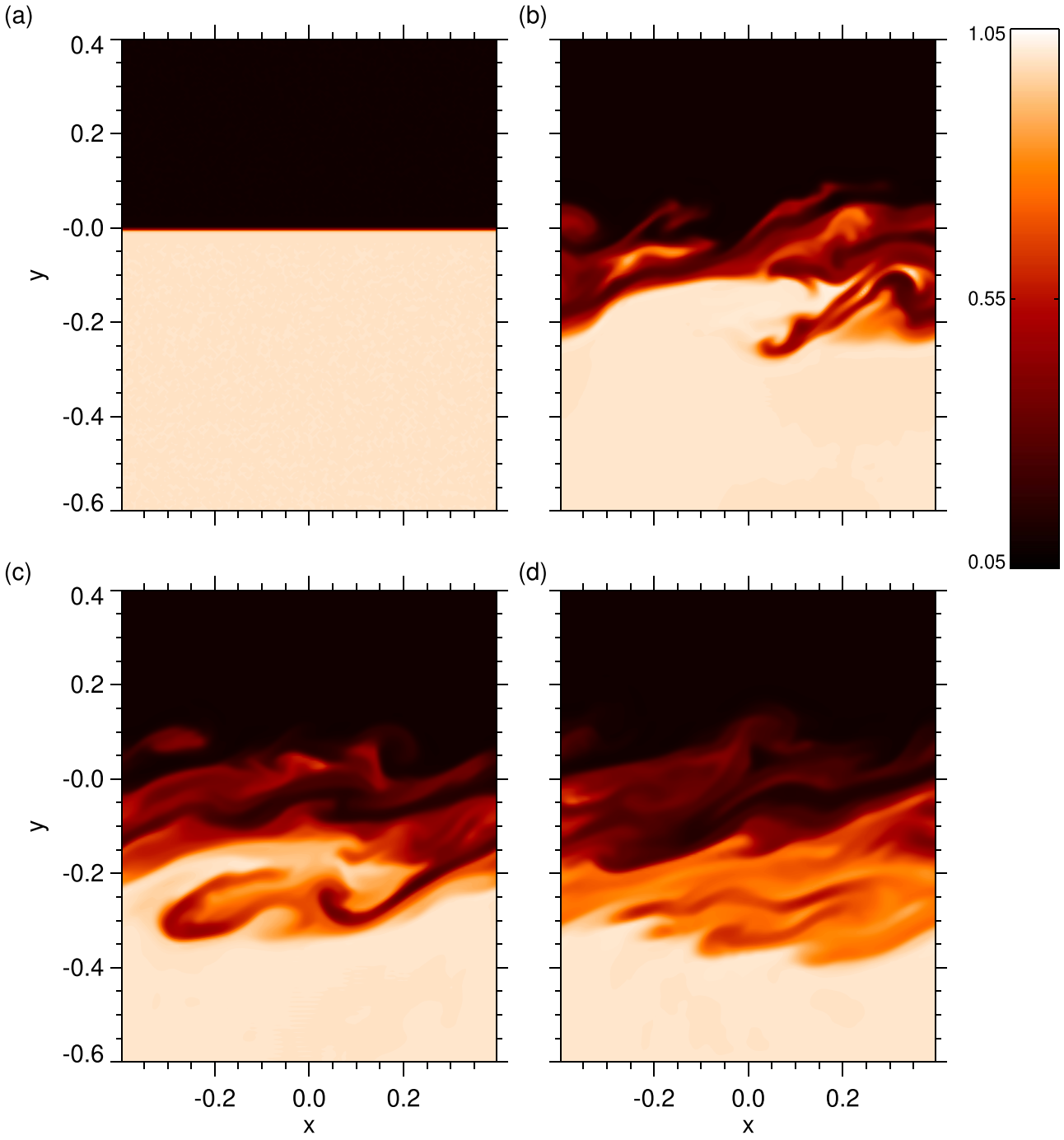

Figure 5. Contour plots of the temperature distribution in the x–y plane, taken at $z = 0$ for $t = 0$, 20, 40, and 60, respectively.

Together, these uniquely determine the position of the mixing layer associated with the minimum mean velocity. Visually, it seems that the predicted shift is a good representation of the shift in the mixing layer from the $y = 0$ position.

Panel (a) of Figure 6 gives the profile of $\langle\rho\rangle$ against y. The red lines show the simplified model used, which is not a perfect representation but does provide a very good estimate of the $\langle\rho\rangle$ distribution. Calculating from the simulation, the mean density across the whole mixing layer gives a value of $\overline{\rho} = 3.21$. The predicted density from the model for the simulation parameters is $\rho_{\rm mixed} = \sqrt{10} \sim 3.16$, which is a difference of less than 2%. This small difference can be understood by the slight extension of the mixing layer on the right-hand side resulting in slightly more mass existing in the layer than predicted. Therefore, both the total mass and the spatial distribution of $\langle\rho\rangle$ are well-represented.

Panel (b) of Figure 6 gives the distribution of $\langle v_{\rm x}\rangle$ against y. The model for this quantity is shown in red, and this provides a reasonably accurate model of the velocity profile. We can also see that the bounds on the mixing layer for this quantity are accurate.

Looking at panel (c) of Figure 6, which shows the kinetic energy of the mean flow, this energy goes to zero in the center of the mixing layer. The energy that has been removed from the mean flow is 0.58 of the initial energy available in the mixing region. The red line in the panel shows the model prediction for

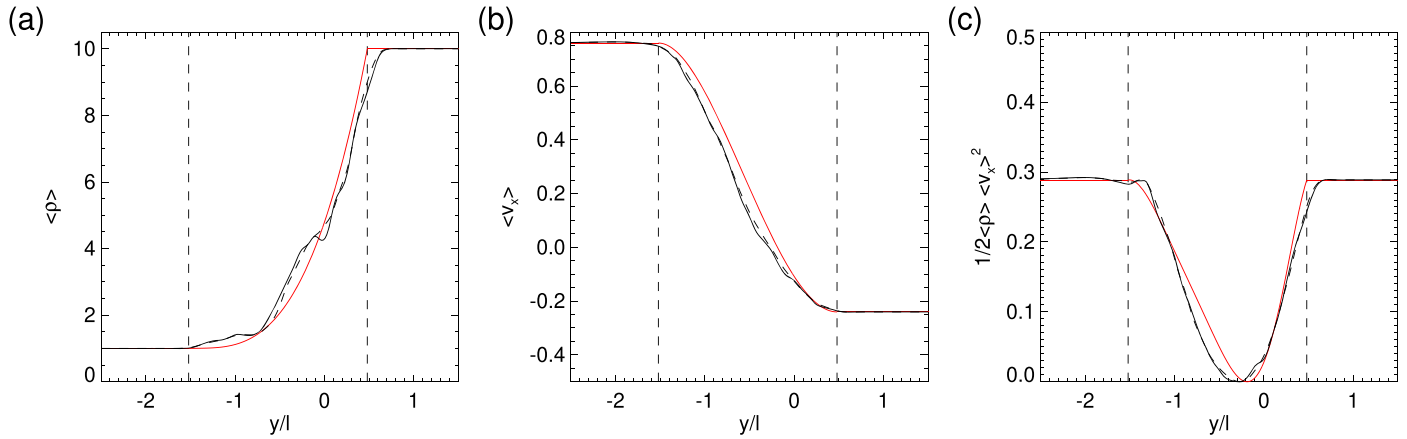

Figure 6. Plots of the mean density $\langle\rho\rangle$ (a), mean velocity $\langle v_x\rangle$ (b), and mean kinetic energy $1/2\langle\rho\rangle\langle v_x\rangle^2$ (c). The solid black curves give the simulation results at $t = 60$, the dashed black curves give the output averaged at $4\tau_D$ intervals between $t = 40$ and $t = 60$, and the solid red lines show the model. The vertical dashed lines give the range of the model mixing layer.

the kinetic energy of the mean flow. The model predicts that 0.53 of the total energy that exists in the mean flow initially in the mixing layer has disappeared from the kinetic energy of the mean flow. The distribution is narrower than the simulation results, leading to the small underestimation. However, this confirms that our model can provide a sufficiently accurate representation of the energy available for turbulent motions—and with this heating, in the nonlinear stages of the instability. The dashed black lines in the panels of this figure show the profiles achieved when time averaging is considered along with spatial averaging. Though this appears to marginally improve the (already good) match between the model and the simulation results, the fact that the match is still not perfect highlights that there are still constraints that exist but are not yet considered in this model.

Figure 7 shows the distribution of the turbulent energy (i.e., the energy held in the velocity and magnetic field fluctuations) normalized by the initial kinetic energy density in the zero-momentum frame of the mixing layer at four separate times during the simulation ($t = 30$, 40, 50, and 60). The trend over time is that the magnitude of the turbulent energy decreases. This is a clear signature of the dissipation of the turbulent energy.

Figure 8 shows the magnitude of the pressure fluctuations $\langle\Delta p\rangle$ from $p_{\rm mixed}$ (normalized by $p_{\rm mixed}$, which in the case of this simulation $=1/\gamma = 0.6$) taken at $t = 60$. As can be seen, the increase in the pressure that results from dissipation and any compressible effects peaks at approximately 2% of $p_{\rm mixed}$. The horizontal dashed red line gives the value of the average pressure increase from heating of the model as given in Equation (34), which is calculated as ~0.017. This line can be seen as a fair visual estimate of the average increase of the pressure through heating. The actual value of $\overline{\Delta p}/p_{\rm mixed}$ from the simulation is $\overline{\Delta p}/p_{\rm mixed} = 0.014$. This is less than the prediction, but as there is still turbulent energy that can be dissipated (see Figure 7), this could rise further over time. Ultimately, due to the marginally increased extraction of mean energy in the simulation, we would expect it to reach a value slightly above that of the model. Nonetheless, the prediction is a fair reflection of the increase in internal energy in the mixing layer. The clear conclusion from this is that the temperature of the mixing layer in the simulation is determined by the mixing process and not by any heating in the simulation (see also Section 4.3).

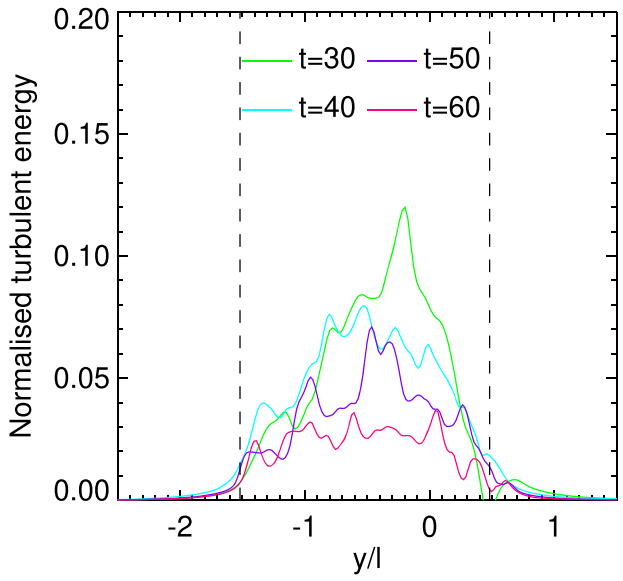

Figure 7. The y distribution of the turbulent energy held in both the velocity and magnetic field fluctuations (averaged in both the x and z directions). This is plotted for a number of separate times, showing that the energy in these fluctuations is decreasing, i.e., that energy is being dissipated. Vertical dashed lines give the extent of the mixing region in the model.

4. Application to Prominence Observations—Mixing versus Heating

To apply the results of the model presented in Section 2 to the observations of Okamoto et al. (2015), we need to use some characteristic values for the temperature, density, and velocity. We use 10^{-15} g cm^{-3} and 10^6 K for the coronal density and temperature, and 10^{-13} g cm^{-3} and 10^4 K for the density and temperature of the prominence thread, which means that we take a constant pressure between the two regions. We also consider shear flows of magnitude 10 km s^{-1}.

The first step is to assess the thermodynamic properties expected of a mixing layer between prominence material and the corona. For a Kelvin–Helmholtz mixing layer between these two, the characteristic density of this layer would be $\rho_{\rm mixed} = \sqrt{10^{-13} \times 10^{-15}}$ g cm^{-3} $= 10^{-14}$ g cm^{-3}. The temperature under these conditions is also determined by the

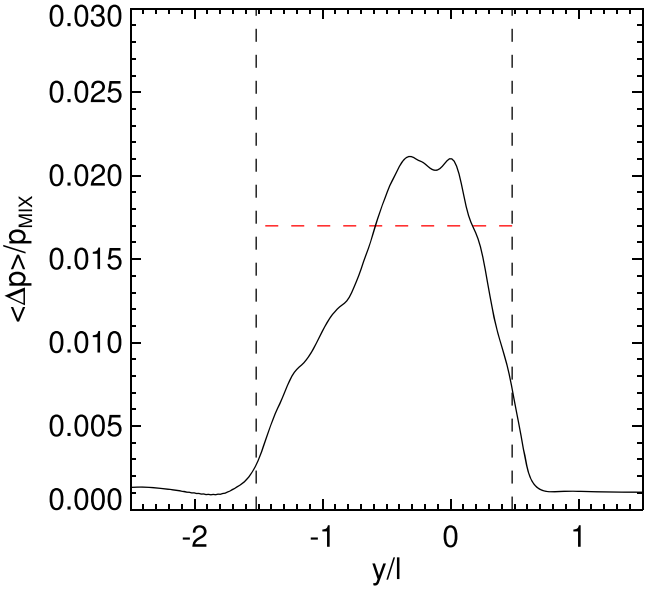

Figure 8. Magnitude of the pressure fluctuations, averaged in the x and z directions, normalized by $p_{\rm mixed}$ at $t = 60$. Vertical dashed lines give the extent of the mixing region in the model. The horizontal dashed red line gives the predicted increase in pressure as a result of turbulent heating.

geometric mean, so $T_{\rm mixed} = \sqrt{10^4 \times 10^6}$ K $= 10^5$ K. When this process is observed in the cool ($\sim 10^4$ K) and warm ($\sim 10^5$ K) passbands of IRIS, this mixing would result in cool material being removed by the mixing resulting in high-intensity material disappearing from that passband. As the warmer material forms in the mixing region, intensity would increase in warm passbands. This could be expected to observationally lead to the thinning of the prominence thread in cool lines, with a thickening of the transition region of the prominence thread when observed in warm lines.

It is worth noting that, to achieve the mixing temperatures predicted by this model, locally the plasma has to relax from the two different particle distributions that make up the prominence and coronal plasmas to a single distribution that is at transition region densities and temperatures. In MHD simulations, a single Maxwellian distribution in each pixel is assumed to form instantaneously, but for the prominence corona system, it takes sufficient particle collisions between the cooler and hotter particles to relax to a single temperature particle distribution in a local area.

Along magnetic field lines in the solar corona, thermal conduction can effectively perform this task, but across field lines, the conduction is significantly reduced. To reach the mixing temperatures, heat transport across the magnetic field is essential. To make the mixing across the field more efficient, it is necessary to break the connectivity of the magnetic field in order to allow thermal conduction to transfer heat from the hotter to the cooler components of the mixing layer. As long as the lengths of the field lines hosting the prominence thread are sufficiently longer than the width of the mixing layer (see Equation (47) for an estimate), the instability can wrap up the magnetic fields to produce the reconnection required to allow field-aligned thermal conduction to become important. For a mixing layer 100 km in width, this length would be $L \approx 4 \times 10^3$ km, which is sufficiently small to allow these dynamics to occur on a prominence thread. Due to the formation of many secondary vortices caused by the instability as it nonlinearly develops (meaning smaller scales both along and across the field), the dynamic evolution of the vortices naturally produces many small-scale current sheets (e.g., Antolin et al. 2015). This, in turn, means that reconnection as a result of the vortex evolution can be important for the thermalization of the plasma.

An alternative method by which turbulent heat transport could occur is as a result of the drift of neutral atoms across the magnetic field. In the dense, cool material of prominences, the degree of ionization has not been exactly determined—but ranges of the ionization fraction of 0.2–0.9 (Engvold et al. 1990; Labrosse et al. 2010) or ratios of electron to neutral hydrogen density in the range 0.1–10 (Patsourakos & Vial 2002) have both been reported. The work of Hillier (2019) highlights the role of the motion of neutral particles across the magnetic field for heat transport. As the neutral particles drift across the magnetic field, they can act (through collisional coupling with the local plasma they meet) as a heat sink for the hotter material they interact with, resulting in a transfer of heat. Because the relaxation to a single temperature distribution due to thermal conduction is more effective in the hot, low-density coronal plasma, and the relaxation by ion–neutral drift is more important for regions of the mixing layer that have more cool material, it is likely that both of these mechanisms could be important in this mixing process in the solar corona.

We can use Equation (34) to estimate the heating by the Kelvin–Helmholtz instability of prominence material in the solar corona. For this, we can use a velocity shear of 10 km s^{-1}, and for a temperature of 10^5 K, the sound speed is 33 km s^{-1}. Combining these with the appropriate densities, this would give an increase in temperature of the fluid of $\Delta T < 0.003 T_{\rm mixed}$. That is to say, the energy available for rapid heating via turbulent dissipation can possibly result in a temperature increase that is only a fraction of a percent of the temperature achieved through mixing, i.e., the possible heating is not significant compared to the mixing in this situation, because there is just not enough energy available for dissipation.

Using the estimate for the timescale given in Equation (35), we can estimate the observable timescales for these processes. Taking a mixing region of half-width 100 km would result in a lower estimate for both the mixing timescale and the heating timescale of $\sim$100 s (note that this increases linearly with increases in the half-width). Based on the dominance of mixing, it would be sensible to assume that this process would take a few hundreds of seconds to significantly reduce the cool intensity of a prominence thread while producing the warmer material at a similar rate. Combining this timescale with the total energy available for dissipation gives an energy dissipation rate of $\sim 10^{-4}$ erg cm^{-3} s^{-1}. Note that this is much larger than the 10^{-8} erg cm^{-3} s^{-1} estimated for quiescent prominence turbulence by Hillier et al. (2017), though this difference is mostly due to the localization assumed for the turbulence in this study and the larger velocities used.

4.1. Radiative Losses and the Possibility of Coronal Cooling

One important consequence of the dominant role of mixing is that, while it does not efficiently heat the system, it does alter the temperature of the plasma, changing the radiative losses. As shown in Figure 2 of Anzer & Heinzel (2008), for example, the loss function $\Lambda(T)$ for optically thin radiative losses for coronal plasma at constant pressure varies with temperature, with the total radiative losses given by $R = n^2 \Lambda(T)$ (where n is the

number density). For the mixing of cool (10^4 K) prominence plasma with hot (10^6 K) coronal plasma, the characteristic temperature of the mixing layer is 10^5 K. Their calculations show that the radiative losses from the mixing region are going to be greater than the losses for either of the plasmas before mixing.

For the coronal plasma we are using, the timescale for radiative loss is approximately 10^3 s, and for the prominence plasma, this becomes approximately 1 s (though it should be noted that the use of optically thin radiation to model the optically thick radiative losses of the prominence strongly underestimates this timescale). The result of the mixing gives a timescale of approximately 1 s for what will be an optically thin plasma, which equates to an energy loss rate of $\sim 0.1\,\mathrm{erg\,cm^{-3}\,s^{-1}}$. Therefore, the cooling times have been drastically reduced by mixing. When compared to the heating rate as a result of turbulence, it is clear that the cooling rate dominates this, meaning that even though there is heating occurring, thermal energy is being lost from the system as a result of the Kelvin–Helmholtz instability occurring faster than it is being replaced. Therefore, the overall result of the mixing process is more likely to be cooling of the solar corona, rather than heating.

It is important to note that the estimates for the change in the radiative losses presented above were calculated using ρ_{mixed} and T_{mixed}. However, these are just characteristic values for the mixing layer, and as shown in Figure 3 for large density contrasts, the density—and with it, the temperature—has a nonlinear distribution across the mixing layer. Therefore, these estimates should only be taken as characteristic values to highlight how the cooling timescale of the prominence corona system will evolve as a result of the KHi.

This estimate of the cooling time is based on the fluids having become well-mixed, but even before this process has taken place, i.e., in the early stages of the instability when vortices are forming but the fluids remain relatively distinct, it is likely that the radiative losses of the prominence–corona system would increase. The high-temperature component of this system is optically thin, so the corrugation of the boundary between the two fluids does not change the losses from this material. However, the optically thick emission from the prominence material is determined in part by the surface area through which the photons can escape; see the shell emission found for optically thick lines from radiative transfer models of simulations presented in Figure 8 of Okamoto et al. (2015).

Taking the linear instability to have reached a displacement of the boundary of $1/k$, i.e., the instability will be developing nonlinearities (e.g., Hillier 2019), and using the plane wave solution of the linear instability (so we can assume a sine wave form of the boundary displacement), the surface area of the boundary increases by approximately 25%. Using the results from Anzer & Heinzel (2000), the energy flux from the prominence material as a result of radiative losses is $\sim 3 \times 10^4\,\mathrm{erg\,cm^{-2}\,s^{-1}}$. Therefore, the radiative losses from a prominence thread of thickness 10^8 cm with the instability growing on a scale of 10^7 cm would approximately increase the radiative losses per unit length of the prominence thread from 2×10^{13} to $2.5 \times 10^{13}\,\mathrm{erg\,cm^{-1}\,s^{-1}}$ (assuming all the losses are from optically thick lines). Though this is not as effective as the large radiative losses that occur once mixing is fully developed, it does highlight that the increase in radiative losses can occur through all stages of the instability.

The example using prominence material embedded in the solar corona has a large temperature difference, and as such, the possible heating by the KHi is limited. However, coronal loops are of a temperature and density similar to those of the ambient corona. In this situation, as the density contrast is small, the heating will be at its most effective, and as the temperature contrast is small, T_{mixed} will not differ greatly for the background temperatures. The latter means that the radiative losses will not be greatly affected, making it possible that heating rates can outstrip loss rates, and the former means that the maximum heating would be given as $\sim M^2/16$, around the most efficient it can be.

4.2. Some Thoughts on Driven Oscillations

In this section, we have focused on the case where the KHi develops as a result of an oscillation that is driven by a impulsive kick and then left to evolve, but another possibility is that an oscillation in a flux tube in the solar atmosphere is being continuously driven at its ends in the photosphere. Assuming that the driven oscillations are not strong enough to completely destroy the structure of the flux tube, there would be a constant energy source to drive instability—and with it, turbulence. This would again create the mixing layer via the KHi process presented in this paper. However, we can hypothesize that, once this layer has become large enough compared to the radius of the flux tube, the boundary between the flux tube and the external corona would become sufficiently thick that instabilities cannot grow. This can be seen in our simulations (see panel d of Figure 5) where even though there is still shear flow (and with it, free energy that could be used for both mixing and heating), the mixing layer has become sufficiently large compared to the width of the box that it is no longer able to extract more energy from the flow. This implies the existence of geometrical constraints on the absolute thickness of mixing layer on a flux tube. Inside this layer, as there are going to be radial density variations, there is the possibility of resonances between the local Aflvén frequency and the frequency of the large scale oscillation, which may allow further, localized excitation of the KHi—and with that, further dissipation as discussed in Terradas et al. (2008).

Another aspect to consider is the timescale of the mixing (given in Equation (33)). This is limited by the velocity shear (shorter for larger shears) and by the density contrast (longer for larger contrasts), so it is easy to conceive cases where the timescale for mixing (and with it heating) is longer than the characteristic timescale for energy input into the flux tube. This can be mitigated by energy being injected only at the relatively small cross section of the footpoints of a flux tube, in contrast with the large regions on the flanks of a flux tube that can be dissipating energy via the KHi. This implies that, even if the characteristic timescale for energy dissipation is longer, a larger region is involved in the dissipation, meaning the total energy input into oscillating flows of the flux tube and the total energy extracted from these flows can balance. However, when this is not the case, there are three possibilities: other dissipation mechanisms dominate, the excess energy leaks from the tube, or (in the case the driver is resonant with the flux tube kink frequency), the oscillations get larger and larger until the KHi heating timescale matches the energy input timescale.

4.3. Differentiating between Heating and Mixing in Simulations

When looking at the results of a 3D simulation, especially the incredibly complex simulations of the Kelvin–Helmholtz

instability forming on the surface of oscillating prominence threads, it can be difficult to determine whether features that appear are the result of heating or of mixing. Fortunately, as the mixing solution is based on having no change in internal energy, which implies conservation of pressure, it is possible to estimate the temperature distribution from mixing by just knowing the density distribution.

For the case where the initial pressure profile is constant, it would be expected, based on application of the ideal gas law, that the temperature at any point in the mixing layer as a result of mixing alone is $T \propto 1/\rho$. For a situation where the gas pressure is not constant, this can be more complicated to estimate, but it is possible to determine a linear map between the density and the expected pressure achieved through mixing. The density at any point in the mixing layer can be written as the sum of the fractions of the densities outside the mixing layer given by:

$$\rho = A_1(\boldsymbol{x})\rho_1 + A_2(\boldsymbol{x})\rho_2, \tag{48}$$

where A_1 $(\boldsymbol{x})$+A_2 $(\boldsymbol{x}) = 1$, which allows for A_1 and A_2 to be uniquely determined from simulation data at each point in the mixing layer. This means that the pressure expected from mixing at any point in the mixing layer is given by:

$$p = A_1(\boldsymbol{x})p_1 + A_2(\boldsymbol{x})p_2. \tag{49}$$

Then, using an ideal gas law, the temperature at that point in the mixing layer expected to occur as a result of mixing associated with these values of ρ and p can be determined. By comparing this estimate to the simulated temperature distribution, it is possible to estimate the position and level of the temperature increase by removing the influence of the mixing.

To highlight this, we have applied these arguments to our simulations. This is presented in Figure 9, where the difference between the local temperature of the plasma and the temperature estimated using the mixing arguments (all normalized by the estimated temperature) is plotted for a slice in the simulation at $z = 0$. In the KHi layer, there are areas where heating (either through compression or dissipation) has lead to temperature increases. However, the magnitude of these increases only reaches to the level of ~2.5% of the temperature the plasma reaches through mixing.

There is a caveat to this estimate, and that comes as a result of compression. The model in the previous paragraphs assumes no change in internal energy, so any change found in internal energy could be attributed to turbulent heating. However, changes in internal energy can come about through work done through compression. If there is an initial pressure jump or the turbulence is large enough to have a noticeable turbulent pressure, there will be a compressive or expansive effect that will alter the temperature from the mixing value—but without being associated with energy dissipation. Therefore, it would always be worth estimating the order of these effects before making the comparison, to make sure the heating estimate is not misleading.

5. Summary and Discussion

In this paper, we have presented a simple phenomenological model for mixing by the magnetic Kelvin–Helmholtz instability in a uniform pressure and magnetic field. The model was constructed using conservation of mass, momentum, and energy, and this has been used to predict the characteristic values of the density, pressure, magnetic field, temperature, velocity, and kinetic energy associated with the mixing layer. The key results are:

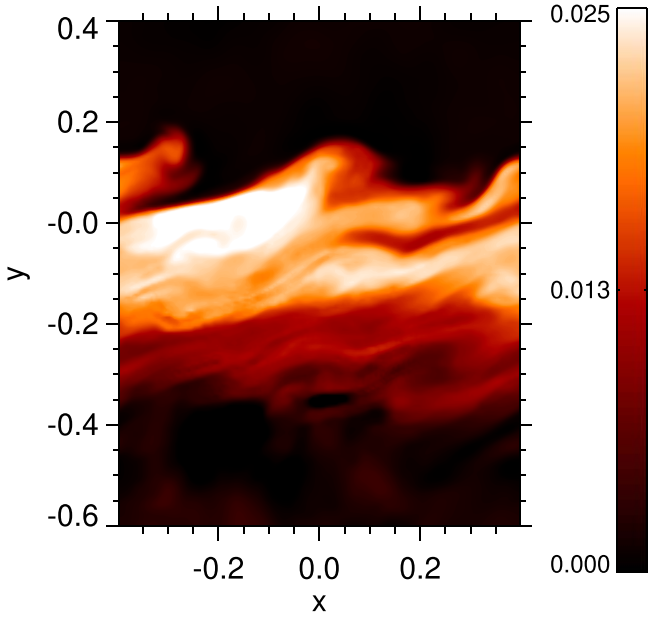

Figure 9. Difference between temperature and mixing temperature normalized by mixing temperature in the KHi layer at $t = 60$.

(i) The central position of the mixing layer is shifted by having a density jump toward the low-density side. The larger the density difference, the larger the shift.

(ii) The characteristic density in this layer is given by $\sqrt{\rho_1\rho_2}$, and the characteristic value of the temperature is $T_{\rm mixed} = \sqrt{T_1 T_2}$.

(iii) The total fluctuating energy can be calculated and used as an estimate for the energy that can be dissipated in the system and is bounded above by $M^2/16$ where M is the Mach number of the flow.

(iv) In flows with high Reynolds numbers, an estimate for the lower bound of the timescale for mixing/heating can be given by:

$$\tau_{\rm mixed} \geqslant \frac{2l}{\Delta V}\sqrt{2}\,\frac{\sqrt{\alpha_1} + \sqrt{\alpha_2}}{(\alpha_1\alpha_2)^{1/4}}, \tag{50}$$

with this also providing an estimate of the dissipation timescale of the system.

(v) The predictions of this model are well-supported by numerical calculations.

Application of this model to the formation of a thick transition region between a cool, high-density region and the hot, tenuous solar corona highlights that it is much more likely for mixing, rather than heating, to drive the observed temperature changes presented in Okamoto et al. (2015). Predictions for the temperature material created by mixing give estimates of 10^5 K. This leads to one of the greatest consequences of Kelvin–Helmholtz instability: the mixing process does not add much heat to the system, but it does greatly increase the efficiency of the radiative losses by creating thick regions at transition region temperatures and densities.

Ultimately, this process makes energy loss from the corona, i.e., coronal cooling, more likely than coronal heating.

The current level of the model does not take into account many possible variations: for example, how oscillatory flow changes the nonlinear evolution (the linear stability problem was investigated in Barbulescu et al. (2019) and Hillier et al. (2019)), or how changes in the gas and magnetic pressure across the shear layer change the mixing process. However, the current model provides sufficiently accurate estimates and scalings for the basic model proposed, based on the conservation of mass, momentum, and energy of the system, so any extension of the model to more complex scenarios will still have the same constraints. Therefore, the general conclusions are likely not to be greatly altered.

One area that is worthy of discussion, though beyond the scope of the current paper, is the influence of a nonpotential magnetic field on the energy released. It can be expected that, as with the kinetic energy, the total of the mean magnetic energy distribution after mixing is smaller than that held in the initial distribution (see Figure 4 for the change in the kinetic energy). Simulations by Howson et al. (2017) numerically investigated this possibility, with their results suggesting that more heating would be possible as a result of the KHi developing in a twisted magnetic field. As such, an important further development for the model we present in this paper is the inclusion of these effects.

The model presented in this paper has been used to investigate the nonlinear MHD Kelvin–Helmholtz instability relating to solar prominences, but all the arguments in Section 2 are equally applicable in the case where $B = 0$, i.e., it also applies to hydrodynamic systems, and to other MHD systems (e.g., the flanks of CMEs (Foullon et al. (2011)). Therefore, though the application of the model looked at in this paper is for the solar atmosphere, the model (along with its promised extensions) will be significantly more versatile in reality, and can be applied to estimate the mixing and heating behavior of any system undergoing the MHD KHi.

A.H. is supported by his STFC Ernest Rutherford Fellowship grant No. ST/L00397X/2 and STFC research grant ST/R000891/1. I.A. acknowledges financial support from the Spanish Ministerio de Ciencia, Innovación y Universidades through project PGC2018-102108-B-I00 and FEDER funds. This work used the DiRAC@Durham facility managed by the Institute for Computational Cosmology on behalf of the STFC DiRAC HPC Facility (www.dirac.ac.uk). The equipment was funded by BEIS capital funding via STFC capital grants ST/P002293/1, ST/R002371/1 and ST/S002502/1, Durham University and STFC operations grant ST/R000832/1. DiRAC is part of the National e-Infrastructure.

ORCID iDs

Andrew Hillier https://orcid.org/0000-0002-0851-5362
Inigo Arregui https://orcid.org/0000-0002-7008-7661

References

Antolin, P., De Moortel, I., Van Doorsselaere, T., & Yokoyama, T. 2016, ApJL, 830, L22
Antolin, P., De Moortel, I., Van Doorsselaere, T., & Yokoyama, T. 2017, ApJ, 836, 219
Antolin, P., Okamoto, T. J., De Pontieu, B., et al. 2015, ApJ, 809, 72
Antolin, P., Schmit, D., Pereira, T. M. D., De Pontieu, B., & De Moortel, I. 2018, ApJ, 856, 44
Antolin, P., Yokoyama, T., & Van Doorsselaere, T. 2014, ApJL, 787, L22
Anzer, U., & Heinzel, P. 2000, A&A, 358, L75
Anzer, U., & Heinzel, P. 2008, A&A, 480, 537
Arregui, I. 2015, RSPTA, 373, 20140261
Barbulescu, M., Ruderman, M. S., Van Doorsselaere, T., & Erdélyi, R. 2019, ApJ, 870, 108
Berger, T., Hillier, A., & Liu, W. 2017, ApJ, 850, 60
Berger, T. E., Shine, R. A., Slater, G. L., et al. 2008, ApJL, 676, L89
Berger, T. E., Slater, G., Hurlburt, N., et al. 2010, ApJ, 716, 1288
Chandrasekhar, S. 1961, Hydrodynamic and Hydromagnetic Stability (Oxford: Clarendon)
De Pontieu, B., Title, A. M., Lemen, J. R., et al. 2014, SoPh, 289, 2733
Engvold, O., Hirayama, T., Leroy, J. L., Priest, E. R., & Tandberg-Hanssen, E. 1990, in Hvar Reference Atmosphere of Quiescent Prominences, ed. V. Ruzdjak & E. Tandberg-Hanssen, Vol. 363 (New York: Springer-Verlag), 294
Foullon, C., Verwichte, E., Nakariakov, V. M., Nykyri, K., & Farrugia, C. J. 2011, ApJL, 729, L8
Goossens, M., Terradas, J., Andries, J., Arregui, I., & Ballester, J. L. 2009, A&A, 503, 213
Hillier, A. 2019, PhPl, 26, 8
Hillier, A., Barker, A., Arregui, I., & Latter, H. 2019, MNRAS, 482, 1143
Hillier, A., Matsumoto, T., & Ichimoto, K. 2017, A&A, 597, A111
Hillier, A., Morton, R. J., & Erdélyi, R. 2013, ApJL, 779, L16
Hillier, A., & Polito, V. 2018, ApJL, 864, L10
Hillier, A., Takasao, S., & Nakamura, N. 2016, A&A, 591, A112
Hollweg, J. V. 1978, SoPh, 56, 305
Howson, T. A., De Moortel, I., & Antolin, P. 2017, A&A, 607, A77
Ionson, J. A. 1978, ApJ, 226, 650
Karampelas, K., Van Doorsselaere, T., & Antolin, P. 2017, A&A, 604, A130
Kelvin, L. 1880, Natur, 23, 45
Labrosse, N., Heinzel, P., Vial, J. C., et al. 2010, SSRv, 151, 243
Magyar, N., & Van Doorsselaere, T. 2016, A&A, 595, A81
Mak, J., Griffiths, S. D., & Hughes, D. W. 2017, PhRvF, 2, 113701
Matsumoto, Y., & Seki, K. 2010, JGRA, 115, A10231
Möstl, U. V., Temmer, M., & Veronig, A. M. 2013, ApJL, 766, L12
Ofman, L., & Thompson, B. J. 2011, ApJL, 734, L11
Okamoto, T. J., Antolin, P., De Pontieu, B., et al. 2015, ApJ, 809, 71
Okamoto, T. J., Tsuneta, S., Berger, T. E., et al. 2007, Sci, 318, 1577
Patsourakos, S., & Vial, J.-C. 2002, SoPh, 208, 253
Rempel, M., Schüssler, M., & Knölker, M. 2009, ApJ, 691, 640
Ryu, D., Jones, T. W., & Frank, A. 2000, ApJ, 545, 475
Ryutova, M., Berger, T., Frank, Z., Tarbell, T., & Title, A. 2010, SoPh, 267, 75
Soler, R., Terradas, J., Oliver, R., Ballester, J. L., & Goossens, M. 2010, ApJ, 712, 875
Stuart, J. T. 1967, JFM, 29, 417
Terradas, J., Andries, J., Goossens, M., et al. 2008, ApJL, 687, L115
Terradas, J., Magyar, N., & Van Doorsselaere, T. 2018, ApJ, 853, 35
Tsuneta, S., Ichimoto, K., Katsukawa, Y., et al. 2008, SoPh, 249, 167
Vallis, G. K. 2017, Atmospheric and Oceanic Fluid Dynamics: Fundamentals and Large-Scale Circulation (2nd ed.; Cambridge: Cambridge Univ. Press), 946
Wentzel, D. G. 1974, SoPh, 39, 129
Wentzel, D. G. 1978, RvGSP, 16, 757
Wentzel, D. G. 1979, ApJ, 233, 756
Winant, C. D., & Browand, F. K. 1974, JFM, 63, 237
Yang, H., Xu, Z., Lim, E.-K., et al. 2018, ApJ, 857, 115